

1 **Human spinal cord organoids exhibiting neural tube morphogenesis for a quantifiable**
2 **drug screening system of neural tube defects**

3

4 Ju-Hyun Lee¹, Hyogeun Shin^{2,3}, Mohammed R. Shaker¹, Hyun Jung Kim¹, June Hoan Kim¹,
5 Namwon Lee⁴, Minjin Kang⁵, Subin Cho⁶, Tae Hwan Kwak⁸, Jong Woon Kim⁹, Mi-Ryong
6 Song¹⁰, Seung-Hae Kwon¹¹, Dong Wook Han⁸, Sanghyuk Lee^{6,7}, Se-Young Choi¹², Im Joo
7 Rhyu¹, Hyun Kim¹, Dongho Geum⁵, Il-Joo Cho^{2,3}, **Woong Sun¹**

8

9 ¹ Department of Anatomy, Brain Korea 21 Plus Program for Biomedical Science, Korea
10 University College of Medicine, Seoul 02841, Republic of Korea

11 ² Center for BioMicrosystems, Brain Science Institute, Korea Institute of Science and
12 Technology (KIST), Seoul 02792, Republic of Korea

13 ³ Division of Bio-Medical Science & Technology, KIST School, Korea University of Science
14 and Technology (UST), Daejeon 34113, Republic of Korea

15 ⁴ InterMinds Inc., Seongnam-si, Gyeonggi-do 03493, Republic of Korea

16 ⁵ Department of Biomedical Sciences, Korea University College of Medicine, Seoul 02841,
17 Republic of Korea

18 ⁶ Department of Bio-Information Science, Ewha Womans University, Seoul 03760, Republic
19 of Korea

20 ⁷ Department of Life Science, Ewha Womans University, Seoul 03760, Republic of Korea

21 ⁸ Department of Stem Cell Biology, School of Medicine, Konkuk University, Seoul 05029,
22 Republic of Korea

23 ⁹ Department of Obstetrics and Gynecology, Chonnam National University Medical School,
24 Gwangju 61469, Republic of Korea.

25 ¹⁰ School of Life Sciences, Gwangju Institute of Science and Technology, Gwangju 61005,
26 Republic of Korea

27 ¹¹ Division of Bio-imaging, Korea Basic Science Institute, Seoul 02841, Republic of Korea

28 ¹² Department of Physiology, Dental Research Institute, Seoul National University School of
29 Dentistry, Seoul 03080, Republic of Korea

30

31

32 **Corresponding author:**

33 Woong Sun, Ph.D.

34 Department of Anatomy, Brain Korea 21 Plus Program for Biomedical Science, Korea
35 University College of Medicine, 73, Incheon-ro, Seongbuk-gu, 02841 Seoul, Republic of Korea

36 E-mail: woongsun@korea.ac.kr

37 Tel: +82-2-2286-1404, Fax: +82-2-929-5696

38 **Abstract**

39 The human spinal cord forms well-organized neural circuits for environment sensing and
40 motor behavior. The three-dimensional (3D) induction of the spinal cord-like tissue from
41 human pluripotent stem cells has been reported, but they often do not mimic morphological
42 features of neurulation and their maturity is limited. Here, we report an advanced 3D culture
43 system for the production of human spinal cord-like organoids (hSCOs) suitable for the scale-
44 up and quantitative studies. The hSCOs exhibited many aspects of spinal cord development,
45 including neurulation-like tube-forming morphogenesis, differentiation of the major spinal
46 cord neurons and glial cells, and mature synaptic functional activities. We further demonstrated
47 that hSCOs platform allowed quantitative and systematic high-throughput examination of the
48 potential risk of neural tube defects induced by antiepileptic drugs. Thus, hSCOs can be used
49 for understanding human spinal cord development, disease modeling, and toxicology screening.

50

51 **Introduction**

52 The spinal cord plays critical roles in the neurotransmission of sensory inputs and motor
53 outputs between the brain and the body, the coordination of central pattern generation, and
54 many sensory-motor reflexes. During embryonic development, the spinal cord is formed via
55 neurulation, an early morphogenetic process. Typically, neurulation is mediated by sequential
56 processes including polarized neuroepithelial (NE) cell induction, sheet-like neural plate
57 formation, and folding-based tube morphogenesis¹. The posterior part of the neural tube
58 develops into the spinal cord containing more than 20 classes of neurons that connect other
59 tissues in the body and establish neuronal circuits governing somatosensation or locomotion²,
60 ³. Thus, many human diseases associated with the spinal cord lead to abnormalities in sensory-
61 motor reflexes and autonomic nervous system. Deficiencies in the early neurulation process
62 often lead to neural tube defects (NTDs). As one of the major congenital malformations, NTDs
63 can be caused by genetic, nutritional, or environmental factors. More than 200 genes are known
64 to cause NTDs in mouse models^{4, 5}. Human genetic studies associated with NTDs have
65 demonstrated limited correlations with mouse mutations. Most of the information about human
66 NTDs is obtained from retrospective clinical research. The primary risk factors for NTDs are
67 folate deficiency, maternal diabetes, and side effects of antiepileptic drugs (AEDs) during
68 pregnancy⁶⁻⁹. A huge gap exists between mouse and human studies. The mechanism by which
69 such factors cause or alter NTD pathology remains primarily unknown.

70 The access to human embryo/fetus is highly limited owing to the ethical and technical
71 limitations. Thus, *in vitro* replication of important features of human embryonic development
72 via three-dimensional (3D) culture of the organoids derived from human pluripotent stem cells

73 (hPSCs) can lead to new opportunities for investigating human development, including three
74 germ layers patterning, early axial organization, and organogenesis¹⁰⁻¹³. The central nervous
75 system (CNS) organoids are considered valuable model systems to explore the most complex
76 and highly organized human nervous system and neurological disorders¹⁴⁻¹⁹. A 3D organoid
77 system representing the posterior part of the CNS has been reported²⁰⁻²⁴. Such protocols
78 demonstrate the efficiency of spinal cell type induction, dorsoventral specification, and 3D
79 trunk neuromuscular connections. Although advent of organoids offer a new paradigm in
80 biomedical research and neurodevelopmental biology, batch variations, intra- or inter-organoid
81 variations have limited their use in robust quantification-based drug screening or toxicology
82 tests^{17, 25, 26}. Morphological and physiological evaluations of the spinal cord organoid system
83 are in the early stages. Thus, the use of these organoids as a drug screening system requires
84 improvement for reducing the inter- or intra-experimental variations and developing accurate
85 quantification systems.

86 Here, we report a novel method for producing spinal cord organoids recapitulating
87 neurulation-like morphogenesis. Most of the previous organoid models exhibited neural-
88 follicle or cyst expansion similar to 2D neural rosette formation, which is different from neural
89 tube formation *in vivo*, attributing limitations to the current culture system for NTD disease
90 modeling. Our 3D culture system can be used for the rapid production of a large number of
91 spinal cord organoids, allowing for the quantification of the organoid morphogenesis. The
92 robustness of the method was evaluated with a screening of the AEDs that can cause NTDs,
93 which can offer insights to understand the mechanism of neurulation and the toxicology test
94 for the human NTDs.

95 **Results**

96 **Protocol for the formation of the human spinal cord organoids (hSCOs)**

97 We established a 3D culture system that recapitulates early spinal cord induction with the
98 morphological events of neurulation (Fig. 1a). Our protocol included three consecutive steps.
99 In the first step, the WNT activator CHIR99021 (CHIR) and the inhibitor of TGF- β signaling
100 SB431542 (SB) were added to the hPSCs monolayer culture for 3 days to induce neural stem
101 cells (NSCs)²⁷. During the 2D induction process, hPSCs were determined as caudal neural stem
102 cells (cNSCs) at the neuromesodermal progenitors (NMps) stage, as observed in embryonic
103 caudal neurogenesis *in vivo*²⁸ (Supplementary Fig. 1a-d). Next, cNSC colonies were gently
104 detached from the dish to form 3D sphere. These spheres were cultured in the presence of bFGF
105 for 4 days for the expansion and establishment of the neuroepithelial (NE) alignment
106 (Supplementary Fig. 1e, f and Supplementary Video 1). Lastly, the media was changed to favor
107 cell specification and morphogenesis by removing bFGF and adding retinoic acid (RA). With
108 this, spheroids underwent morphogenesis resembling neural tube formation. Such
109 morphological conversions were easily visible under a transmission light microscope (Fig. 1b
110 and Supplementary Video 2).

111 Using the high-resolution 3D volume imaging method based on the tissue-clearing technique,
112 we visualized the key characteristics of the organoid at each stage (Fig. 1c and Supplementary
113 Video 3). In the presence of bFGF in step 2, the organoids established a distinct, columnar
114 morphology of the NE surface layer exhibiting apical polarity (morphological stage I).
115 Tracking the morphology of individual cells demonstrated a surface layer with an elongated

116 pseudostratified columnar architecture (Fig. 1d). These cells exhibited the NE marker ZIC2²⁹
117 and established apical polarity similar to the embryonic neural plate, such as apical localization
118 of phospho-Myosin Light Chain (pMLC) (Fig. 1e). While the partial establishment of basal
119 lamina in some organoids was observed, the basal lamina formation may not be essential for
120 further morphogenesis as this feature was not prominent in certain organoids that underwent
121 proper morphogenesis.

122 When the medium was replaced with -bFGF/+RA condition as a last step, round and
123 symmetric spheroids began to fold (morphological stage II) (Fig. 1c, f, and Supplementary Fig.
124 2a). This process exhibited some features of neural folding *in vivo* in the perspective of
125 morphogenesis. Along the apical side with an accumulation of cell-cell junctional proteins, the
126 neural plate is gradually elevated and generate neural groove-like structures. At the cellular
127 levels, the middle point cells in the neural groove showed the wedge-like cell morphology with
128 condensed tubulin at the apical side (Fig. 1g and Supplementary Video 4). However, these
129 wedge-like cells failed to express floor plate marker FOXA2 (Supplementary Fig. 2b),
130 suggesting that the cellular differentiation and morphological alteration at the hinge points can
131 be segregated. Although such NE layers in the organoid were not associated with any non-
132 neuronal cells (Supplementary Fig. 2c), they exhibited a cytosolic bridge and strong clustering
133 of occludin (Fig. 1h, i)³⁰. The pMLC distributed laterally with planar cell polarity (PCP),
134 producing cellular forces promoting neural folding, as noted *in vivo*³¹ (Fig. 1j and
135 Supplementary Fig. 2d-f). Scanning electron microscope images revealed the clear
136 morphological change was observed at each stage in the organoid, especially at neural fold
137 stage (morphological stage II), showing the continuum of groove-like neural folds and

138 internalizing neural tube (Fig. 1k and Supplementary Fig. 2g). When tube morphogenesis was
139 completed, the internalized neural tube exhibited an elongated tubular morphology, which was
140 visualized by the apical localization of ZO-1 and pH3-expressing mitotic cells (morphological
141 stage III) (Fig. 1l and Supplementary Video 5). They exhibited radial alignment of cells with
142 apical polarity (Fig. 1m) and neural differentiation patterning by NEUN (Fig. 1n). The
143 importance of cell polarity was further explored. The perturbation of cell polarization by the
144 Rock inhibitor Y-27632 blocked apical polarity, and suppressed tube-forming morphogenesis
145 (Supplementary Fig. 3a-c). Embedding the 3D spheroids into the matrigel rapidly inverted the
146 polarity of the NE cells, and promoted morphogenesis resembling the rosette expansion-based
147 ventricle formation as previously reported in brain organoid protocol^{14, 18, 19} (Supplementary
148 Fig. 3d-f). We also verified this protocol with 4 different hPSC lines and consistently observed
149 similar morphogenesis (Supplementary Fig. 4).

150

151 **Transcriptome analyses of hSCO maturation**

152 Transcriptomic analysis was performed to evaluate the progress of hSCO maturation after
153 initial morphogenesis period. The microarray dataset demonstrated a progress increase
154 similarity in the global gene expression profiles between hSCOs and human fetal spinal cord
155 tissue (Fig. 2a). Gene Ontology (GO) analysis demonstrated that neural stem cell proliferation
156 and patterning-related genes were mainly expressed in the early stage hSCOS, while
157 maturation-related gene clusters such as neurogenesis and gliogenesis were upregulated in late
158 stage (Fig. 2b). To better understand the cell type specification of hSCOs at the single cell level,

159 droplet-based single-cell RNA sequencing of 1-month hSCOs was performed with 11,038 cells.
160 The clustering analysis was performed based on the representative transcription factors that
161 identify the dorsal/ventral subclass cell types in spinal cord. The hSCOs included both mitotic
162 and post-mitotic cells composed of approximate dorsoventral identity, mainly with the V0
163 domain cells (Fig. 2c, d and Supplementary Fig. 5a). hSCOs exhibited posterior identity
164 indicated by HOX code associated with the cervical-thoracic level supporting their spinal cord
165 identity (Supplementary Fig. 5b). While the domain-specific marker staining confirmed the
166 presence of these cells in the hSCOs (Supplementary Fig. 6a), their regional patterning was not
167 evident (Supplementary Fig. 6c). However, by treatments with dorsal inducer BMP4 or ventral
168 inducer sonic hedgehog (SHH) agonist Purmorphamine hSCOs accordingly switched toward
169 their domain identity, suggesting that they maintain the potential to form dorsoventral
170 specification in response to the external morphogen stimuli. Thus, upon dissection of chick
171 notochord as the source of ventral inducer and the treatment of recombinant BMP4,
172 dorsoventral patterning was successfully established as observed by the position of chick
173 notochord (Supplementary Fig. 6b-d). Re-clustering analysis according to the
174 neurotransmitters identified 5 major clusters, namely, neural progenitors (SOX2),
175 glutamatergic neurons (SLC17A6), glutamatergic/cholinergic neurons (SLC18A3),
176 GABAergic neurons (GAD1), GABA/glycinergic neurons (SLC6A5), and other less-defined
177 neuroblasts (DCX) (Fig. 2e-g, Supplementary Fig. 7).

178

179 **Morphological and cellular maturation of hSCOs**

180 In the long-term culture, hSCOs grew and formed histological features of nerve-enriched
181 shell and the cell-enriched core regions (Fig. 3a, Supplementary Fig. 8a and Supplementary
182 Video 6). Consistent with the CNS development procedure, gliogenesis appeared to occur later,
183 as early glial progenitor first seen by the 1-month and mature glial markers evident by 2-month
184 (Fig. 3a,b and Supplementary Fig. 8b). Myelinating oligodendrocytes were also observed in
185 mature organoids (Fig. 2c, d and Supplementary Fig. 8c).

186 After >2 months, hSCOs exhibited V2a glutamatergic interneurons co-expressing LHX3 and
187 CHX10, known as the reticulospinal neurons for locomotor functions³² (Fig. 3e). As shown in
188 Fig. 2, both GABAergic (GABA+) and glutamatergic (vGLUT1+) interneurons were found
189 with adjacent localization (Fig. 3f). Consistent with the specification of the GABAergic
190 subtype during the development process *in vivo*³³, Calbindin+ interneurons acquired
191 heterogeneity, co-expressing other calcium-binding proteins such as calretinin and/or
192 parvalbumin (Fig. 3g-h). Calbindin-expressing interneurons (Renshaw cells) formed contacts
193 with nearby motor neurons—a typical neural network in the spinal cord for the reciprocal
194 inhibition of motor neurons for pattern generation of alternate movements³⁴ (Fig. 3i).
195 Cholinergic neuron fibers (ChAT and VACHT) demonstrated a tendency to run on the surface
196 of the hSCOs (Fig. 3j). When the hSCOs were co-cultured with differentiated human skeletal
197 muscle myotubes, the outgrowing motor fibers had the potential to form neuromuscular
198 junctions (NMJs) observed by labeling with α -bungarotoxin (α -Btx; Fig. 3k and Supplementary
199 Fig. 9a-b). When hSCOs were co-cultured with dorsal root ganglions (DRGs) derived from
200 Tau-GFP transgenic mice, sensory fibers from DRG were observed to readily penetrate the
201 organoids, indicating that hSCOs can receive peripheral sensory input (Supplementary Fig. 9c-

202 e). The neurons in the mature hSCOs exhibited a mature dendritic morphology with spine
203 formation (Fig. 3l) and the expression of mature neuronal markers such as PSD95 and SYN1
204 (Fig. 3m) providing morphological evidence of synaptic contacts. In summary, our hSCOs
205 demonstrated a transcriptional and histological similarity with the spinal cord *in vivo*.

206

207 **Spontaneous and evoked neuronal activity in spinal cord organoids**

208 To evaluate the functional properties of mature hSCOs, we utilized the we utilized a MEMS
209 neural probe embedded with microfluidic channels³⁵. A single silicon neural probe with 16
210 microelectrode arrays was inserted into the middle of hSCOs (Fig. 4a), and the spontaneous
211 neural activity was readily detected (an example of the traces was shown in Fig. 4b). Over time,
212 the spontaneous neural firing/bursting rates increased progressively with highly synchronized
213 neural activity—a typical feature of the developing spinal cord^{36, 37} (Fig. 4c-g and
214 Supplementary Fig. 10a-l). It is noteworthy that burst activities increased rapidly as of 60 days
215 when GFAP⁺ mature astrocytes were observed in hSCOs (Fig. 4e-f). Astrocytes are involved
216 in the modulation of neural networks by regulating synaptic transmission as well as supporting
217 neurons³⁸. Therefore, after the advent of GFAP⁺ mature astrocytes in hSCOs, the rapid increase
218 in burst activity is evidence that a complex functional neural network developed as hSCOs
219 matured. Also, signal synchronization between the electrodes increased as the neural network
220 expanded (Fig. 4g). After measurements of spontaneous neural activity under basal condition,
221 we focally infused drugs during the recording via an outlet located in the silicon neural probe
222 with a drug delivery channel for chemical modulation. Application of the voltage-sensitive

223 sodium channel blocker tetrodotoxin (TTX) significantly suppressed the firing rate, thereby
224 confirming that the electrical signals were a result of neuronal action potentials (Fig. 4h).
225 Treatments with the AMPA receptor antagonist 6-cyano-7-nitroquinoxaline-2,3-dione (CNQX)
226 and the NMDA receptor antagonist (2R)-amino-5-phosphonovaleric acid (AP5) significantly
227 decreased the neural firing rate (Fig. 4i), confirming the excitatory synaptic transmission in
228 hSCO. Treatment with GABA receptor antagonist bicuculline significantly increased the firing
229 rate (Fig. 4j), while GABA receptor agonist baclofen decreased the neural firing rate (Fig. 4k),
230 confirming the inhibitory synaptic transmission in hSCOs. Moreover, the infusion of Calcitonin
231 gene-related peptide (CGRP) that activates spinal dorsal sensory interneurons significantly
232 increased the neural firing rate, suggesting the functional maturation of sensory interneurons
233 within hSCOs (Fig. 4l).

234 Finally, we examined whether hSCOs exhibited neuronal plasticity, which is defined as the
235 ability of the neurons to change network responses to previous intrinsic or extrinsic
236 stimulations³⁹. In 2-month hSCOs, the electrically-evoked activity showed a gradual increase
237 in the action potential based on the repetition of electrical stimulations (Fig. 4m and
238 Supplementary Fig. 10m). Short-term plasticity (STP) was evident as shown by the increase of
239 field excitatory postsynaptic potential (fEPSP) slopes after high-frequency stimulation (HFS)
240 (Fig. 4n and o). Taken together, these data suggest that the ‘learnable’ neural networks are well
241 established with excitatory and inhibitory neural circuits within the hSCOs.

242

243 **Quantification of the effects of antiepileptic drugs (AEDs) on the tube morphogenesis in**

244 **hSCO model**

245 Finally, we tested whether the hSCO model can be used for drug screening or as a toxicology
246 test platform. To improve the reproducibility of the organoid and make it suitable for the
247 quantifiable assay of the tube morphogenesis, we optimized the procedure for 96-well plate-
248 based high content analysis. After the initial induction of cNSCs in 2D, cells were dissociated
249 into single cells, and a defined number of cells were seeded (Fig. 5a). The dissociated cells
250 rapidly re-aggregated and re-established the outer NE layer, which is recognizable by the
251 distinct nuclear alignments (Fig. 5b). As expected, the diameter increased with the cell seeding
252 number, but NE thickness was not affected by the cell seeding number (Fig. 5c). In all sizes,
253 the folding morphogenesis initiated similarly, but larger hSCOs spent longer period to complete
254 morphogenesis (Fig. 5d-f and Supplementary Fig. 11a). Next, we evaluated the effects of the
255 duration of bFGF treatment on the morphogenesis (Fig. 5g). By increasing the duration of
256 bFGF treatments, both hSCO size and NE thickness were increased (Fig. 5h and i). hSCOs
257 with a thicker NE layer spent longer time to initiate neural folding, and often failed to complete
258 tube morphogenesis (Fig. 5j-l and Supplementary Fig. 11b). These data indicate that the
259 kinetics of tube morphogenesis are tunable by modulation of initial cell number and the
260 duration of bFGF treatment.

261 As the morphogenetic process can be imaged, we employed deep learning-based image
262 analysis tools as a cost-effective and automated analysis system. For the establishment of an
263 automated analysis system, we prepared a “pre-labeled” dataset comprising approximately
264 2000 organoids and trained an algorithm with supervised learning to automatically classify the
265 stage of morphogenesis (Fig. 6a). In summary, this framework includes 1) An automatic

266 imaging system that tracks the individual morphogenesis of each organoid in 96-well plates, 2)
267 Deep learning-based classification of the morphogenetic process, and 3) Volume imaging
268 analysis of neural tube structure.

269 To test the proof-of-concept of the system, our platform was analyzed for efficient detection
270 of the effects of AEDs on the NTDs. NTDs are common congenital malformations with a
271 frequency of 0.5–2 per 1,000 pregnancies⁴⁰. Open NTDs, such as spina bifida, are caused by
272 the failure of neural tube closure, which can be a result of genetic mutations or environmental
273 factors^{5, 41}. Especially, AEDs increase the risk of the development of NTDs in humans^{9, 42}. To
274 validate our approach, hSCOs were treated with three different concentrations of 6 selected
275 AEDs, including valproic acid (VPA), carbamazepine (CBZ), phenytoin (PHT), primidone
276 (PMD), lamotrigine (LMG), and gabapentin (GBP). On day 15 following the 8-day treatment
277 of AEDs, VPA- and CBZ-treated groups exhibited a failure of neural tube closure in a dose-
278 dependent manner, while others exhibited normal morphogenesis (Fig. 6c). The heatmap
279 images based on the proportion of NT showed that the initiation of morphogenesis was retarded
280 by the VPA or CBZ treatments, resulting in the delay or failure of tube closure (Fig. 6d and
281 Supplementary table). High-resolution 3D imaging with ZO1 as an apical neural tube marker
282 confirmed that the NTD-like phenotypes developed in response to VPA or CBZ treatments such
283 as incomplete closure and increased branching of the internalized tube structures (Fig. 6e, f and
284 Supplementary Video 7). These results were highly consistent with the reported clinical risks
285 of AEDs, in which VPA and CBZ exhibited the highest risk ratio of congenital malformation,
286 primarily NTDs⁴². Thus, the hSCOs-based toxicology system can recognize the effects of drugs
287 on early neural development, such as the development of NTDs.

288 Discussion

289 Here, we established a robust and quantifiable method for the production of hSCOs via
290 neurulation-like morphological processes. While organoids representing a specific part of the
291 CNS have been reported, they grow via rosette¹⁴⁻¹⁷ or incomplete folding formation¹⁹ with
292 subsequent expansion of ventricles, whose morphogenesis is similar to follicular enlargement.
293 However, our protocol allowed the tube-like morphogenesis resembling the neural tube
294 formation *in vivo*. The prolonged culture of the hSCOs drove the organoids toward the
295 development of the spinal cord. They exhibited the emergence of the spinal cord-type neurons
296 and glial cells, and synaptic network activity. While studies have reported spinal cord-like
297 organoids or neural tubes^{11, 20-24, 43-45}, no study has comprehensively examined the later
298 maturation steps. Particularly with the employment of a nanoelectrode system,
299 electrophysiological properties of hSCOs were easily detectable. We optimized the protocol
300 for culturing individual organoids to quantifiably assess the morphogenesis process, and the
301 robustness of the protocol was successfully demonstrated by the quantifiable examination of
302 the effects of drugs on the tube morphogenesis. Since hSCOs further mature into spinal cord-
303 like neural circuits, our current culture system will provide a valuable opportunity for large-
304 scale analysis of the development and function of human spinal cords *in vitro*.

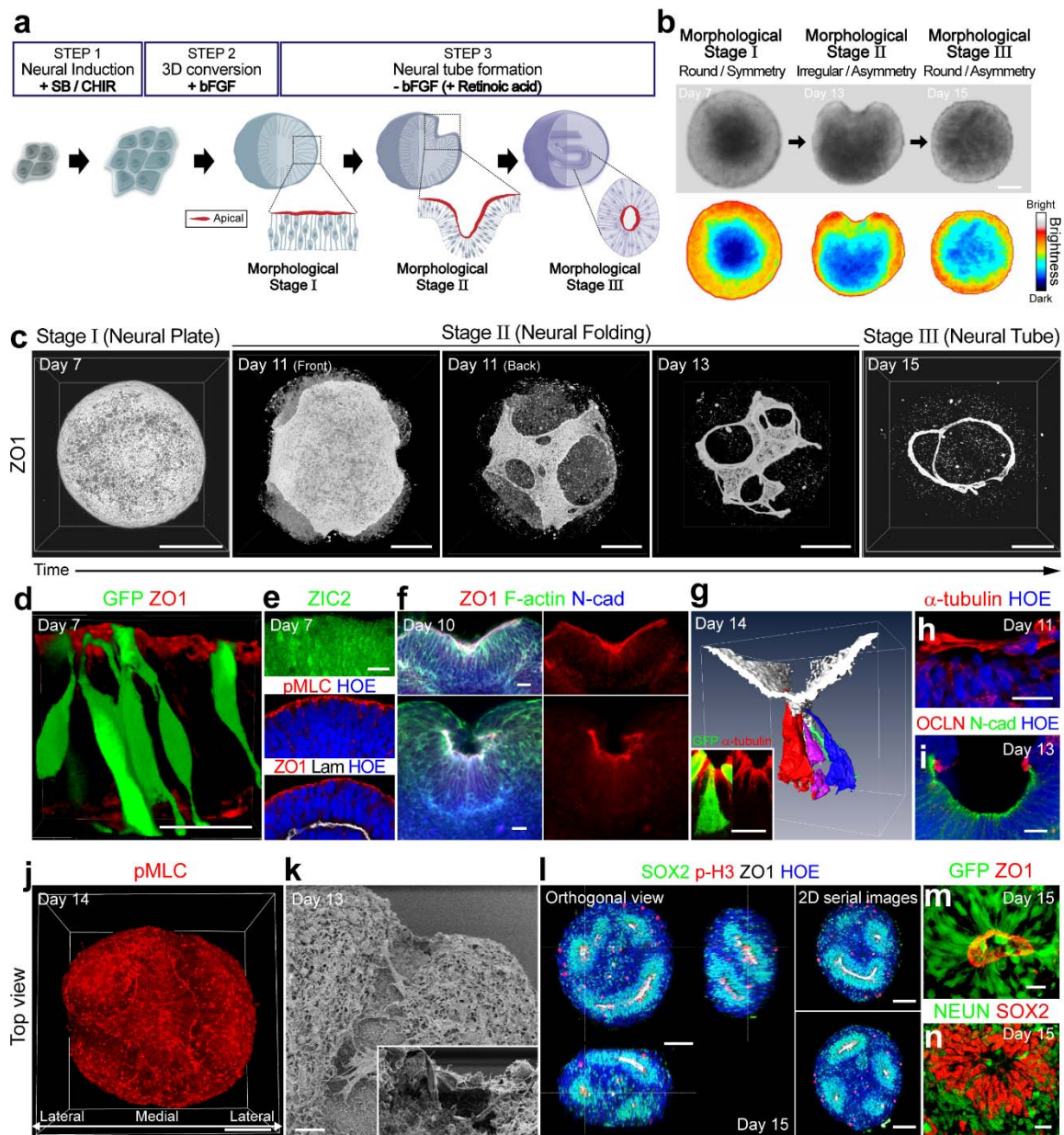
305 The neural tube is an embryonic neural tissue, which leads to the development of CNS¹. It
306 develops through an early developmental process called neurulation, a complex yet ordered
307 process of neural cell specification and morphogenesis that includes early induction of the
308 neural plate, neural fold formation, and neural tube closure. In early embryonic tissue *in vivo*,
309 the neural plate is a planar structure connected to the surface ectoderm. In this model, the neural

310 plate-like structures emerged as a surface layer of the entire 3D sphere. This neural plate-like
311 layers exhibited proper apicobasal and planar cell polarities similar to the neural plate *in vivo*,
312 which is essential for initiating tube morphogenesis that occurs by symmetry breaking. The
313 hSCOs do not contain any non-neural tissue components, such as non-neural epithelia or
314 mesodermal tissues. The core neurulation program is influenced by the surrounding non-neural
315 tissues such as notochord and non-neural epithelia. However, very few studies have examined
316 the contribution of NE cells and other surrounding tissues for neurulation, rendering the
317 conclusion elusive⁴⁶⁻⁴⁸. NE layer underwent tube morphogenesis without the non-neural
318 components in hSCOs. Therefore, it may represent a self-organizing process of NE. This
319 finding is consistent with observations based on many organoids in which epithelial linings can
320 form unique tissue architectures without mesenchymal support⁴⁹.

321 Although hSCOs replicated some features of neural tube formation *in vivo*, several
322 differences were observed between the hSCO morphogenesis and *in vivo* neural tube formation.
323 For instance, while we observed wedge-like cells emerging at the base of the folding NE layer
324 undergoing tube formation, they did not exhibit floor plate markers. In addition, *in vivo* neural
325 tube formation is associated with border formation and the induction of neural crest progenitors.
326 However, we failed to identify neural crest lineage induction. Also, hSCOs *per se* did not
327 exhibit dorsoventral patterning, although they responded to the supplements with chick
328 notochord and treatment with dorsal induction signal BMP4. We speculate that these
329 differences are primarily caused by the absence of non-neural components. Thus, this organoid
330 model will help clarify the self-organizing events of NE cells versus the modulatory role of
331 non-neural tissues in neural tube morphogenesis.

332 In the aspect of quantification analysis, this hSCO protocol provides a unique advantage
333 over other protocols generating neural organoids. Many neural organoids are induced from 3D
334 spheroids, and the tissue-organizing centers appear to emerge randomly, resulting in complex
335 repeats of follicular tissue architectures. Although some protocols for dorsal telencephalic
336 organoids offer smaller variations in terms of size and cell compositions^{17, 26, 50}, variations in
337 the organoids developed in many protocols are one of the major problems for the application
338 of organoids in a quantifiable assay system. We induced a neural fate in 2D and re-aggregated
339 the dissociated cells with a defined number, leading the hSCOs to undergo uniform
340 morphogenesis as a “unit”, suitable for the rapid, simple, and accurate quantifiable analyses.
341 The advantage of this protocol includes the ability to produce a large quantity at a time, to
342 control the size and speed of organoid development, and to automate the imaging system
343 tracking individual morphogenesis, particularly suitable for applications such as high-
344 throughput toxicological screening. The use of an AI-based analysis toolkit allowed unbiased
345 drug screening and can be implemented with an automated system. The testing of our system
346 with AEDs shows the potential and reliability of our hSCO model. Considering that NTD has
347 no reliable toxicology tests available, our demonstration is a good example of how neural
348 organoids can be used for drug screening and toxicology tests as new approach methodologies
349 (NAMs).

Figure 1



350

351 **Fig. 1. Generation of human spinal cord organoids (hSCOs) recapitulating neural tube**
 352 **morphogenesis**

353 **a. Schematics of the generation of hSCOs. b. Brightfield (upper) and pseudocolor (bottom)**

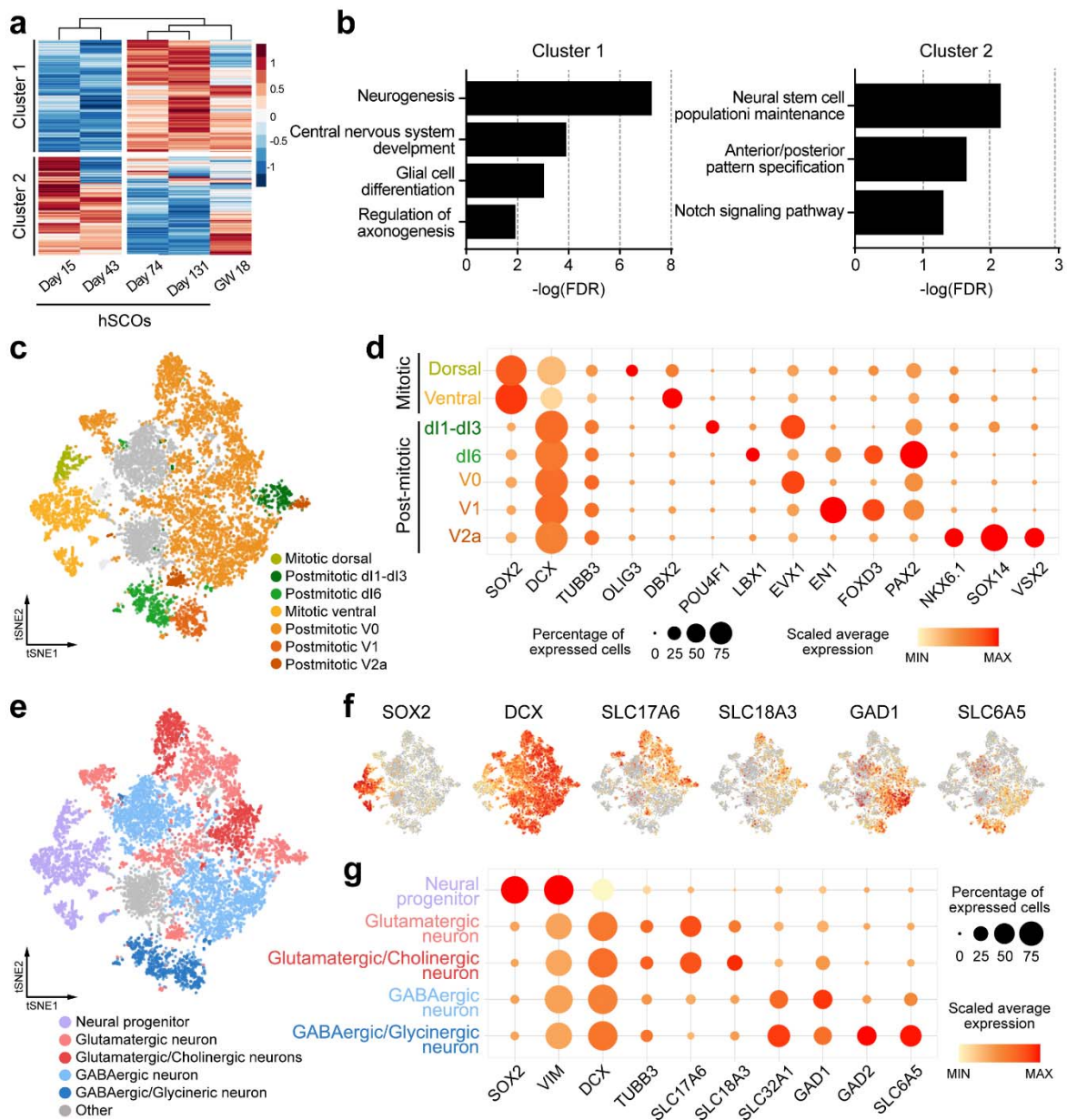
354 images at different stages of hSCO development. Scale bar, 100 μm . **c.** Time-course images of
355 neurulation-like morphogenesis in hSCOs visualized with ZO1 (white) via 3D whole-mount
356 imaging. Scale bar, 100 μm . **d.** Single-cell morphology of the NE layer. A small proportion
357 (5%) of GFP-labeled H9 hESCs were blended with naïve H9 cells to better visualize the
358 morphology of the individual cells. The apical side was labeled with ZO1 (red). Scale bar, 20
359 μm . **e.** Polarization of the NE cells was visualized with staining for ZIC2 (green), pMLC (red),
360 ZO1 (red), and laminin (white). Nuclei were counterstained with Hoechst (blue). Scale bar, 20
361 μm . **f.** Two examples of different modes of neural folding. The upper image shows the hinge
362 formation, and the lower image shows a simple round-up of neural plates. NE was visualized
363 with ZO1 (red), F-actin (green), and N-cad (blue). Scale bar, 20 μm . **g.** Morphology of hinge
364 cells in the hSCOs. Individual-cell morphology was visualized via GFP-labeled H9 cells, the
365 apical side was labeled with ZO1 (white), and 3D images were processed with Amira software.
366 The inset shows GFP+ cells with α -tubulin labeling (red). Scale bar, 20 μm . **h.** The cytosolic
367 bridge is labeled with α -tubulin (red) covering the neural fold. Nuclei were counterstained with
368 Hoechst (HOE, blue). Scale bar, 20 μm . **i.** Localization of OCCLUDIN (OCLN, red) at the
369 dorsal tip of the neural fold. The apical side of the neural fold was labeled with N-cad (green).
370 Scale bar, 20 μm . **j.** Bird eye's view of planar cell polarity of the NE cells visualized via pMLC
371 during fold formation. Scale bar, 20 μm . **k.** SEM images of neural folding-stage hSCOs. The
372 inset shows the position where the neural groove transformed into the neural tube. Scale bar,
373 20 μm . **l.** 3D image of neural tube-stage hSCOs on day 15 of culture. The tube structure was
374 visualized with SOX2 (green) and ZO1 (white) staining. The mitotic cells expressing phospho-
375 histone H3 (p-H3, red) were localized on the apical side of the neural tube. Scale bar, 100 μm .

376 **m.** Single-cell morphology of NE cells in the neural tube. Scale bar, 20 μm . **n.** Double
377 immunostaining for the neural stem cell marker SOX2 (red) and the neuronal marker NEUN
378 (green). Scale bar, 20 μm .

379

380

Figure 2



381

382 **Fig. 2 Transcriptome profiling of hSCOs.**

383 **a.** Heat map analysis of microarray data showing hierarchical clustering of 1556 differentially

384 expressed genes identified from hSCOs and human fetal spinal cord tissue (gestational weeks

21

385 18). **b.** Significantly enriched GO terms related to biological process for upregulated (cluster
386 1) and downregulated (cluster 2) genes. **c.** Two-dimensional tSNE plot of 11,038 cells from 1-
387 month hSCOs by single-cell RNA-sequencing identified by clustering dorsoventral specific
388 cells types. **d.** Gene expression profiles of the dorsoventral specific markers. Circle size and
389 color represent the percentage of expressed cells and the average of gene expression,
390 respectively. **e.** tSNE plot of re-clustered neuronal cell types from (c) datasets. **f.** The
391 distribution of cells expressing the representative neuronal cell marker genes across the main
392 populations. **g.** Gene expression profiles of the neuronal cell markers. Circle size and color
393 represent the percentage of expressed cells and the average of gene expression, respectively.

394

395

396

397

398

399

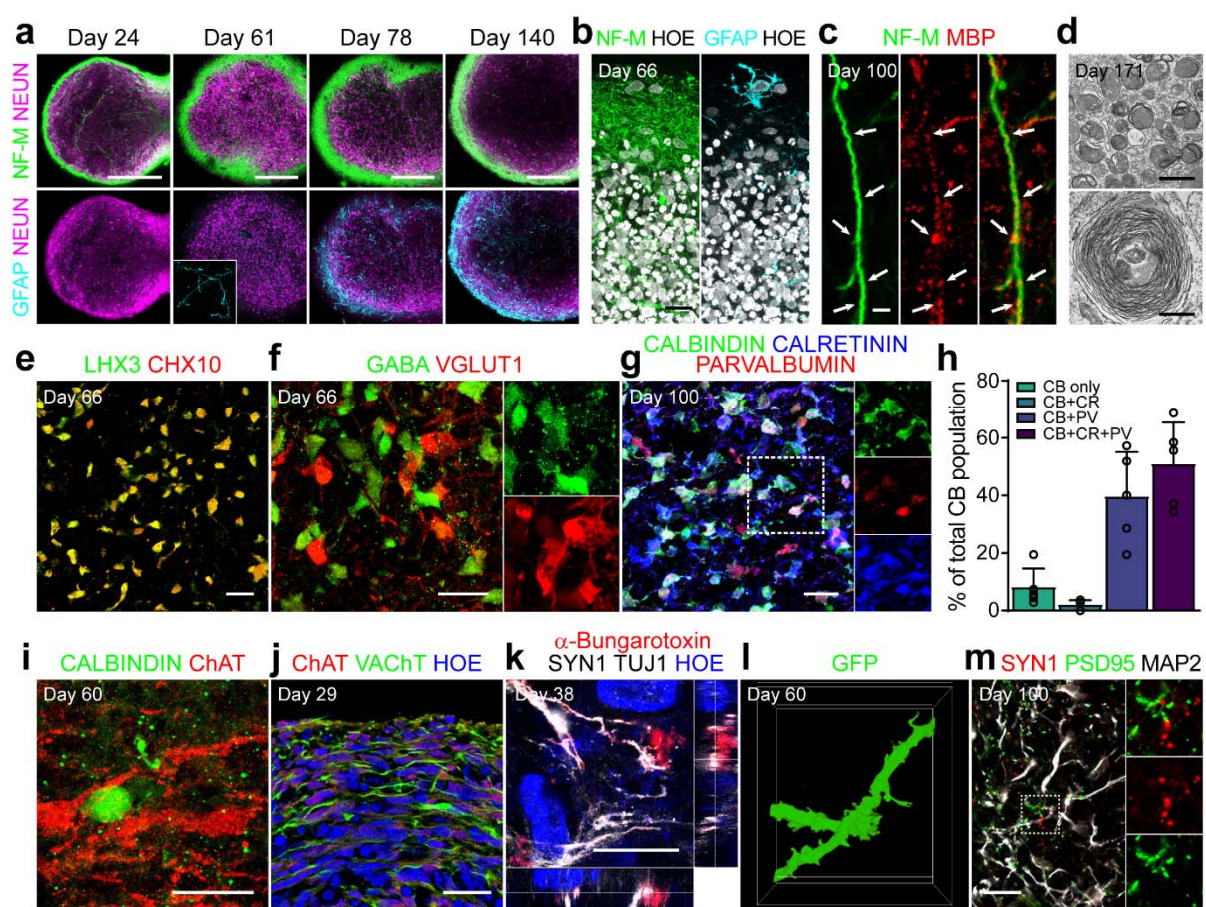
400

401

402

403

Figure 3



404

405 **Fig. 3. Acquisition of spinal cord-like cell fate after long-term culture of hSCOs**

406 **a.** Maturation of hSCOs with structural segregation on the surface with neurite bundles and
 407 central neuronal cell bodies. The samples were stained with NeuN (magenta), Neurofilament-
 408 M (green), and GFAP (cyan). The inset shows the morphology of GFAP-positive astrocytes.
 409 Scale bar, 200 μ m. **b.** High-magnification images on the surface. The samples were stained
 410 with Neurofilament-M (green) and GFAP (cyan). Nuclei were counterstained with Hoechst
 411 (white). **c.** Presence of oligodendrocytes labeled with MBP (red). White arrow indicates a

412 neurofilament-M-labeled fiber (green) that was closely associated with an oligodendrocyte.
413 Scale bar, 2 μ m. **d.** Transmission electron microscopy images for the bundles of nerve fibers
414 and myelination in hSCOs. Scale bar, 500 nm. **e.** Double immunofluorescent labeling of LHX3
415 (green) and CHX 10 (red) on day 66. **f.** Immunostaining for GABAergic (GABA, green) and
416 Glutamatergic neurons (vGLUT1, red) on day 66. **g.** Co-expression of CALBINDIN (CB,
417 green), CALRETININ (CR, blue), and PARVALBUMIN (PV, red) on day 100. The inset shows
418 triple-positive interneurons. **h.** Quantification of CB, CR, and/or PV co-expressing
419 interneurons (error bars indicate s.e.m. n=5). **i.** Presence of Calbindin-expressing Renshaw
420 cells (green) in proximity to ChAT-expressing motor neurons (red). **j.** Cholinergic neuronal
421 axons running on the surface, visualized with staining for ChAT (red) and VAcHt (green). **k.**
422 Establishment of neuromuscular junction of outgrowing motor axons in human myotube co-
423 culture. **l.** The emergence of dendritic spine-like protrusions in the mature neurons of hSCOs.
424 Morphology of the dendrites was traced from GFP-expressing neurons. **m.** Presence of mature
425 synaptic markers, PSD95 (green), SYN1 (red), and MAP2 (blue) in the hSCOs. The inset shows
426 a high-magnification image of the boxed area. All scale bars, 20 μ m, except panel a, c, and d.

427

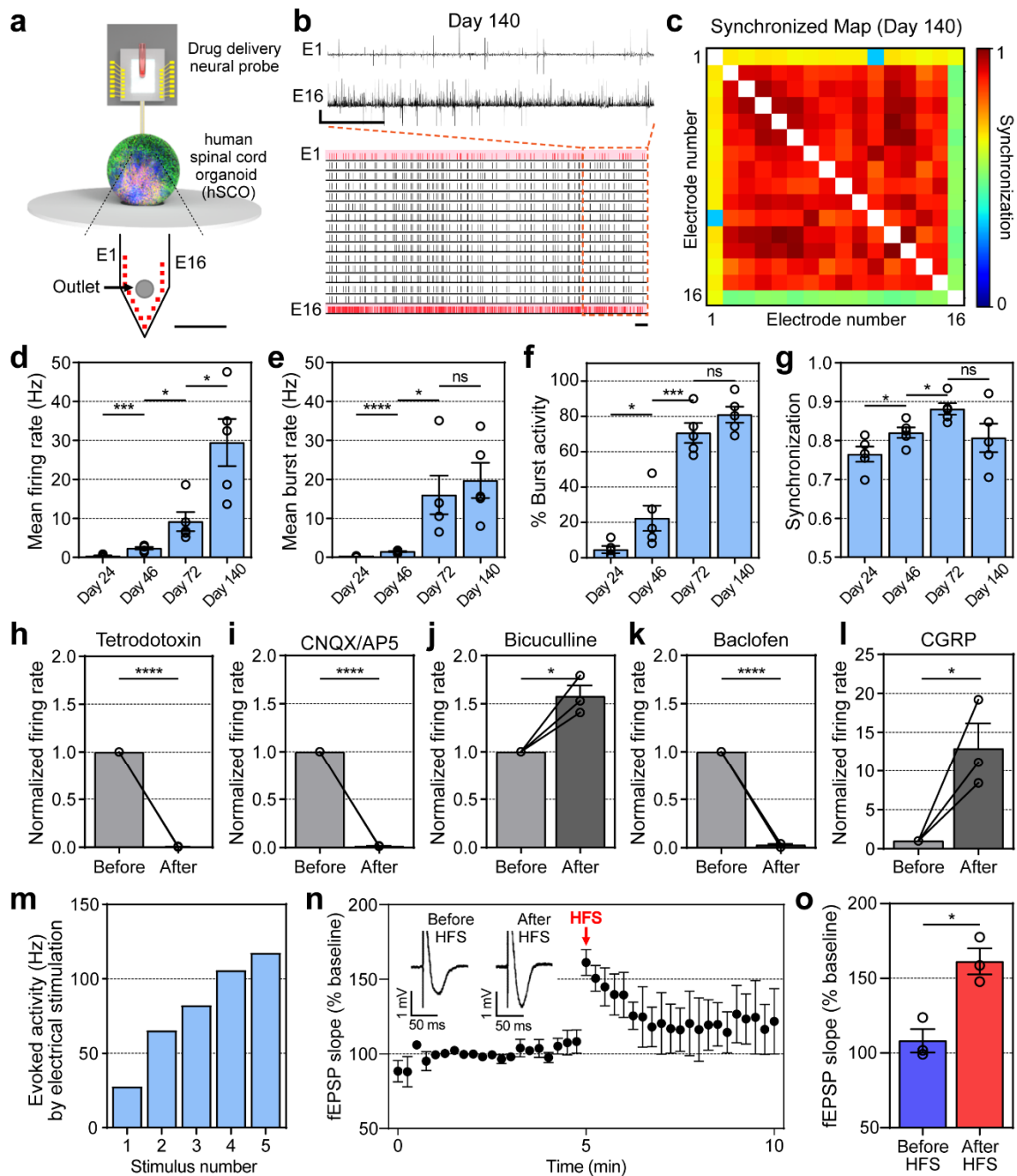
428

429

430

431

Figure 4



432

433 **Fig. 4. Electrophysiological analysis and pharmacological response in hSCOs**

434 **a.** Schematics of extracellular recordings from hSCOs using neural probe with drug delivery
435 capability. Scale bar, 250 μm **b.** The representative raster and transient plot from neural
436 activities recorded in hSCOs at Day 140. Scale bar, 1 sec (horizontal), 1 mV (vertical). **c.** The
437 representative cross-correlation matrices showing synchronization between signal-recorded
438 electrodes from hSCOs at Day 140. **d-g.** Changes in the patterns of neural activity upon hSCO
439 maturation (error bars indicate s.e.m. $n=5$). Mean firing rate (Day 24 – 46: **** P 0.0007; Day 46
440 – 72: * P 0.0244; Day 72 – 140: * P 0.0146; n =number of the samples, Two-tailed unpaired t -
441 test) **(d)**. Mean burst rate (Day 24 – 46: **** P < 0.0001; Day 46 – 72: * P 0.0192; Day 72 –
442 140: ns P 0.5960; n =number of the samples, Two-tailed unpaired t -test) **(e)**. The percentage of
443 burst activity in total activity (Day 24 – 46: * P 0.0445; Day 46 – 72: *** P 0.007; Day 72 –
444 140: ns P 0.1894; n =number of the samples, Two-tailed unpaired t -test) **(f)**. Synchronization
445 between electrodes (Day 24 – 46: * P 0.0467; Day 46 – 72: * P 0.0166; Day 72 – 140: ns P
446 0.0974; n =number of the samples, Two-tailed unpaired t -test) **(g)**. **h-l.** Bar plots showing
447 changes in the mean firing rate before and after drug treatments. 6 μM TTX (before – after: *
448 P 0.0166; n =number of the samples, Two-tailed unpaired t -test) **(h)**. 100 μM CNQX and 100
449 μM AP5 (before – after: * P 0.0469; n =number of the samples, Two-tailed unpaired t -test) **(i)**.
450 10 μM Bicuculline (before – after: * P 0.0285; n =number of the samples, Two-tailed unpaired
451 t -test) **(j)**. 100 μM Baclofen (before – after: * P 0.0301; n = number of the samples, Two-tailed
452 unpaired t -test) **(k)**. 1 μM α -CGRP (before-after: * P 0.0333; n =number of the samples, Two-
453 tailed unpaired t -test, error bars indicated s.e.m. $n=3$ for all) **(l)**. **m.** Firing rate of electrically
454 evoked activities according to stimulus number (The higher the repetition of the stimulus, the
455 higher the increase in firing rate); **n.** Short-term potentiation in the matured hSCOs (error bars

456 indicated s.e.m. n=3 for all; n=number of the sample). **o.** Bar plot showing the comparison of
457 the fEPSP slope right before and after HFS (Before HFS-After HFS: * P 0.0105; n=number of
458 the samples, Two-tailed unpaired *t*-test, error bars indicated s.e.m. n=3 for all);

459

460

461

462

463

464

465

466

467

468

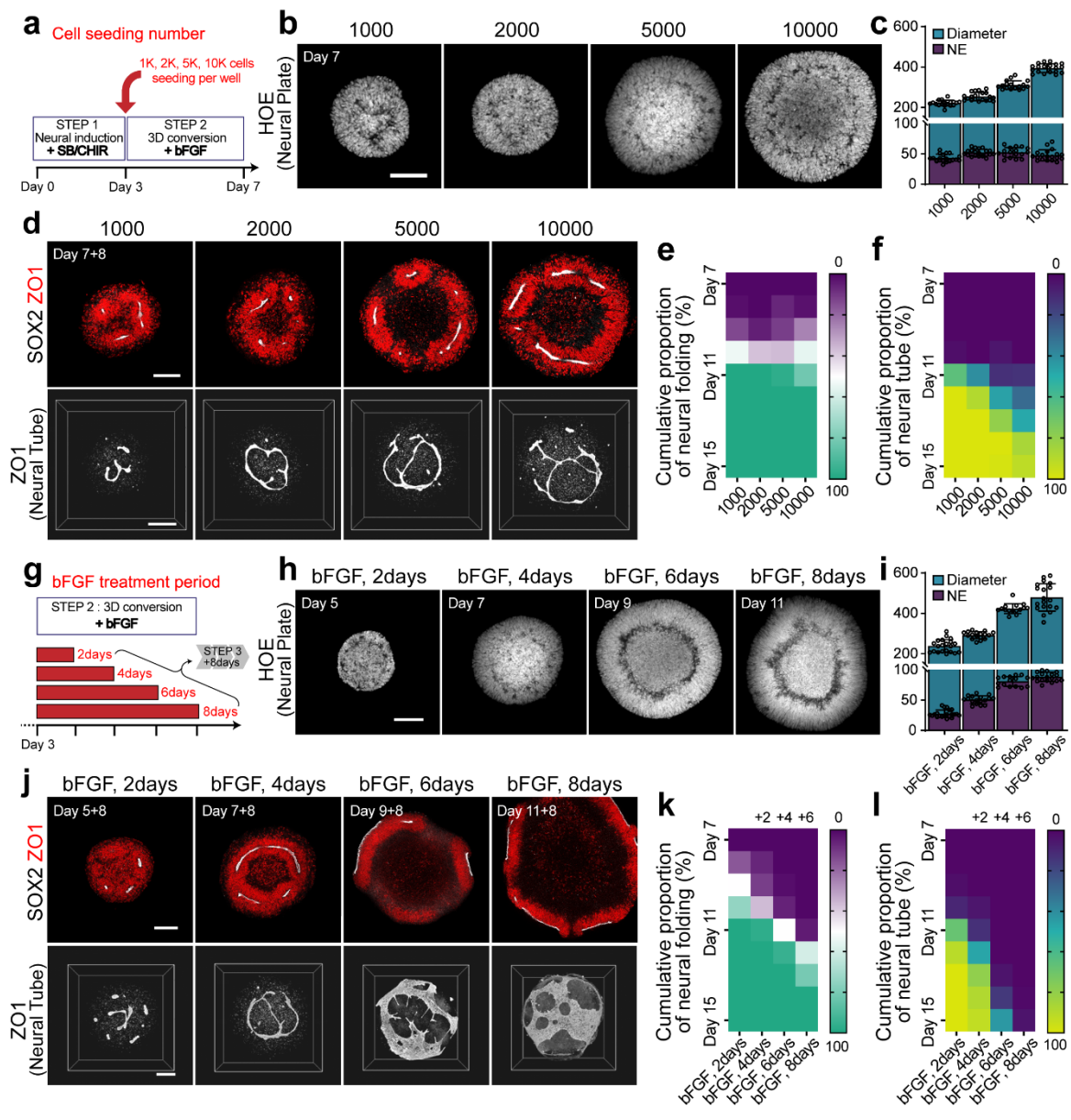
469

470

471

472

Figure 5



473

474 **Fig. 5 Size and bFGF duration-dependent tube morphogenesis in hSCOs**

475 **a.** The experiment scheme to study the effect of different cell seeding numbers on
 476 morphogenesis. **b.** Neural plate formation with different initial cell seeding density. Nuclei

477 were stained with Hoechst (white). **c.** Quantification of the diameter of hSCOs and NE
478 thickness depending on the initial cell seeding numbers. **d.** Neural tube morphology visualized
479 with SOX2 (red) and ZO1 (white) staining on day15. **e-f.** Quantification of morphogenesis with
480 different cell seeding densities. The color of each box indicates the cumulative proportion of
481 the neural folding (**e**) or neural tube (**f**) stage of hSCOs at the indicated culture time. **g.** The
482 experiment scheme to examine the effect of bFGF treatment durations. **h.** Neural plate
483 formation with different bFGF treatment durations. Nuclei were stained with Hoechst (white).
484 **i.** Quantification of the diameter of individual hSCOs and NE thickness depending on the
485 duration of bFGF treatments. **j.** Neural plate/tube morphology visualized with SOX2 (red) and
486 ZO1 (white) staining. **k-l.** Quantification of tube morphogenesis with increasing duration of
487 bFGF treatments. The color of each box indicates the proportion of cumulative neural folding
488 (**k**) or neural tube (**l**) stage of hSCOs at the indicated culture intervals. All scale bars, 100 μ m.

489

490

491

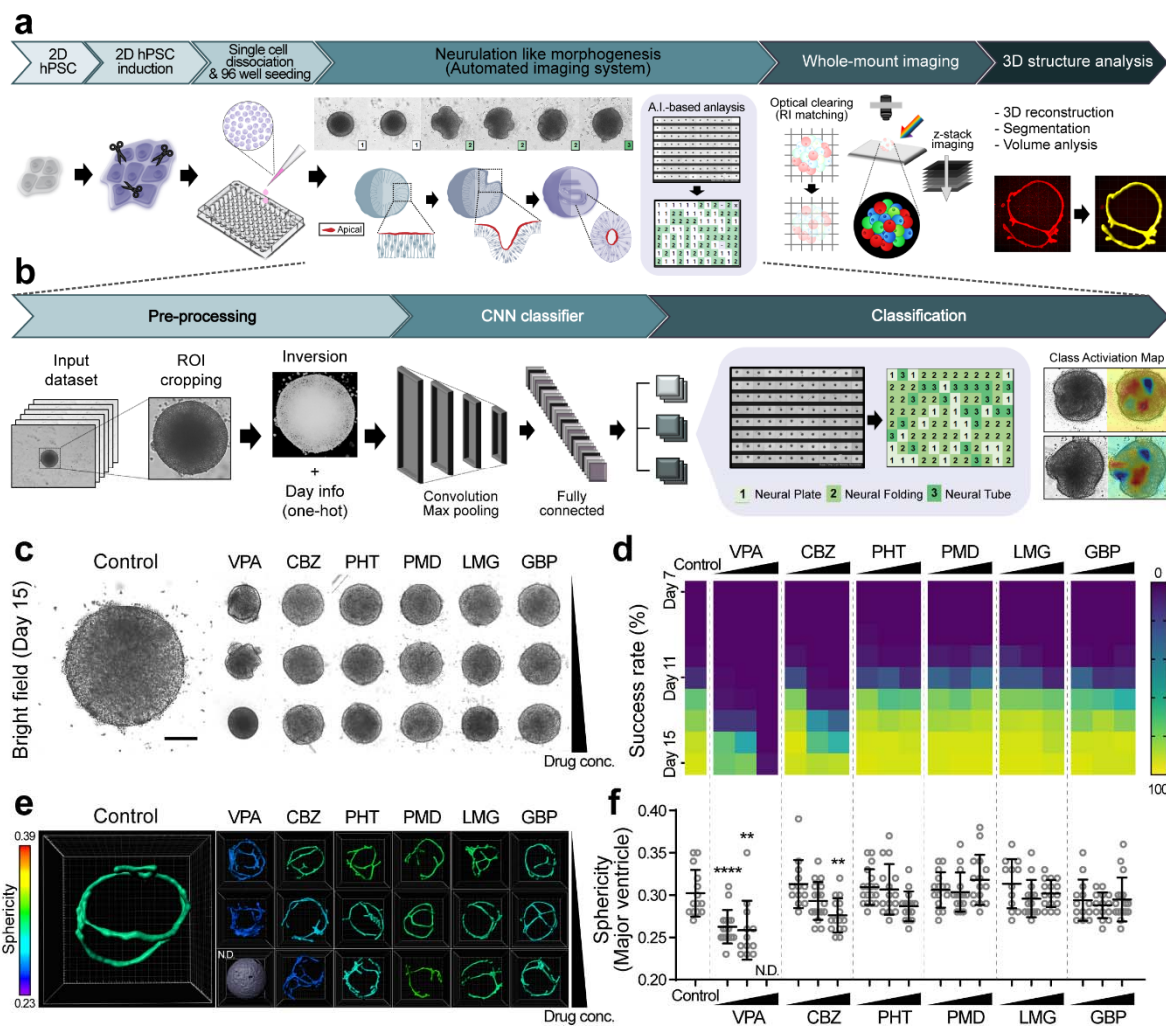
492

493

494

495

Figure 6



496

497 **Fig. 6. Modeling of antiepileptic drug-induced NTDs in hSCOs using deep learning-based**
 498 **classification**

499 **a.** The workflow of an optimized protocol for the quantitative analysis of the neurulation-like
 500 process. After re-seeding the dissociated cells into a microwell (96-well) plate, the morphology
 501 of each organoid was captured with a 1-day interval using an automated imaging system. **b.**
 502 Training procedure for a supervised machine learning model. Based on the bright field images

503 acquired in panel (a), the morphogenic stages (I: Neural Plate, II: Neural Folding, III: Neural
504 Tube) were scored and further analyzed. **c.** Bright-field images of drug-treated hSCOs on day
505 15. Scale bar, 100 μm . **d.** Quantification of morphogenesis after treatments with six different
506 AEDs. Each box shows the proportion of hSCOs exhibiting the neural tube. **e.** 3D neural tube
507 morphology was labeled with ZO1 staining after treatments with six different AEDs. Pseudo-
508 color is based on the sphericity value, which is calculated by the volume and surface area. **f.**
509 Scatter dot plots for the individual sphericity of 3D neural tube measured by ZO1-labeled
510 lumens. (Control – VPA low dose: **** $P < 0.0001$, $n=16$; Control – VPA middle dose: ** $P =$
511 0.0015 , $n=12$; Control – CBZ high dose: ** $P = 0.0069$, $n=15$; n =number of the samples, Two-
512 tailed unpaired t -test)

513

514

515

516

517

518

519

520

521

522 **Methods**

523 **Human PSC Culture**

524 Human H9-GFP ESCs were modified from H9 ESCs by lentiviral mediated insertion of a
525 GFP-expressing cassette into the cellular genome, followed by colony selection. Human iPSCs
526 #5-1 were derived from epidermal fibroblasts, and #56-2 were derived from peripheral blood
527 monocytes. Human iPSCs AICS-0023 were purchased from Coriell Institute. Human PSCs
528 were maintained on matrigel (BD Biosciences, 354277)-coated plates in E8 medium
529 (STEMCELL Technologies, 05990) for hESCs or mTeSR1 (STEMCELL Technologies, 85850)
530 for hiPSCs. The hESCs and hiPSCs were maintained under 5% CO₂ at 37°C with daily media
531 change and were passaged every 5 to 7 days by ReLeSR (STEMCELL Technologies, 05872)
532 into small clumps and replated onto the precoated culture dishes. Experiments were performed
533 on hiPSCs below passage 50.

534

535 **Generation of human spinal cord organoids**

536 To generate human spinal cord organoids (hSCOs), dissociated small clumps of hPSCs were
537 plated onto matrigel-coated plates at high density in mTeSR1. After cell attachment, mTeSR1
538 was replaced with the differentiation medium (DM) consisting of DMEM/F-12. To promote
539 the induction of caudal neural stem cells, hPSCs were treated with SB431542 and CHIR99021
540 in DM for 3 days with daily media change²⁷. On day 3, intact colonies were gently detached
541 from dish. Detached colonies were then transferred onto uncoated culture dishes in DM

542 supplemented with basic fibroblast growth factor (bFGF). They began forming a
543 neuroepithelial (NE) structure at the peripheral surface of the organoid and were fed daily for
544 4 days. On day 7, hSCOs were cultured in the DM containing retinoic acid (RA) without bFGF
545 for 8 days, inducing neural plate morphogenesis in NEs to form the neural tube. The medium
546 was changed every other day. To disrupt cell polarity, the hSCOs were cultured in DM
547 containing Y27632 (10 μ M, Tocris, 1254) for 4 days or embedded within a matrigel in DM for
548 3 days (following the formation of a spheroid on day 4) with daily media change. Brightfield
549 images were acquired with an EVOS microscope (Life Technologies) to observe morphological
550 alterations during neural plate morphogenesis. For maturation, hSCOs were grown in 1:1
551 mixture of DMEM/F-12 and neurobasal medium. The medium was changed every 3 to 5 days.

552 A standard protocol was followed using 96-microwell plates. On day 3 of differentiation, the
553 attached cells were dissociated with Accutase (Innovative Cell Technologies, AT-104). To
554 observe morphogenesis under optimal conditions, the dissociated cells were seeded onto a 96-
555 well low attachment plate (5000 cells per well) in DM supplemented with 20 ng/mL bFGF. The
556 hSCOs in the microplate were fed daily for 4 days. On day 7, hSCOs were cultured in DM
557 containing retinoic acid (RA) without bFGF for 8 days. To induce neural tube defects by AEDs,
558 the hSCOs were either cultured in DM containing AEDs (valproic acid, 0.5 or 1 or 2 mM,
559 Sigma, P4543; carbamazepine, 5 or 50 or 100 μ M, Sigma, C4024; phenytoin, 3 or 30 or 100
560 μ M, Sigma, D4007; lamotrigine, 30 or 100 or 300 μ M, Tocris, 1611; primidone, 5 or 50 or 150
561 μ M, Tocris, 0830; gabapentin, 10 or 300 or 100 μ M, Tocris, 0806). The medium was changed
562 every day. Brightfield images were automatically acquired with JuLi™Stage (NanoEntek) to
563 quantify the rate of neural plate morphogenesis.

564

565 **Tissue clearing and 3D imaging**

566 For 3D volume imaging, hSCOs were fixed with 4% paraformaldehyde (PFA, Biosesang)
567 for 30 min (< 500 μm diameter) or 1 h (> 500 μm), followed by washing several times with
568 PBST (0.1% Triton X-100 in PBS), and incubating with a blocking solution (6% BSA, 0.2%
569 Triton X-100, and 0.01% sodium azide in PBS) overnight. For 3D wholemount
570 immunostaining, hSCOs were immersed in primary antibodies diluted in blocking solution for
571 48 h (Antibodies and their dilutions are listed in Table S1). The primary antibody was then
572 washed with PBST thrice for 10 min. Subsequently, hSCOs were incubated with the
573 appropriate secondary antibody and Hoechst33342 diluted in a blocking solution for 48 h. The
574 organoids were then washed with PBST thrice for 10 min and mounted onto the coverglass (24
575 x 40 mm) with a mounting solution (25% urea and 65% sucrose in H₂O) for optical clearing.
576 All steps were performed in a 0.6 mL tube or 0.2 mL tube with gentle shaking at RT. All images
577 were captured with a Leica TCS SP8 Confocal microscope.

578

579 **3D Image processing and volumetric analysis**

580 For 3D imaging and analysis of hSCOs, raw images were collected using Leica SP8 and
581 processed with LAS X software (Leica). The 3D images of hSCOs were created using Z-stacks
582 (typically 50–300 images) with 0.5–2 μm intervals, and then manually segmented and rendered
583 with the AMIRA software (Thermo Fisher). The regions of interest (ROI) were manually

584 defined based on the intensity of images. For volumetric analysis of neural tube, raw images
585 were rendered with the IMARIS software (OXFORD Instruments). The segmentation of ROIs
586 was performed by intensity-based thresholding with labeled ZO1. The 3D structural
587 quantification including parameters such as sphericity, volume, and surface area were
588 calculated by the IMARIS software. The sphericity (Ψ ; $\pi^{1/3}(6V)^{2/3}A^{-1}$) was calculated by the
589 volume (V) of ZO1 particles and its surface area (A).

590

591 **Histology and immunofluorescence**

592 The hSCOs were fixed by immersion in 4% PFA overnight at 4°C and washed several times
593 in PBS. The samples were then incubated with 30% sucrose in PBS at 4°C until completely
594 submersed, embedded in Tissue-Tek Optimal Cutting Temperature (O.C.T. Compound,
595 SAKURA), frozen on dry ice, cryosectioned serially to obtain 16- to 40- μ m thickness and
596 collected onto New Silane IIWE coating slides (Muto Pure Chemicals Co. Ltd, 5118-20F). For
597 immunostaining, samples were permeabilized with PBS thrice with 5 min durations at RT,
598 blocked with a solution (3% BSA and 0.2% Triton X-100 in PBS) for 30 min at RT, and
599 incubated with the respective primary antibody diluted in a blocking solution overnight at 4°C.
600 (Antibodies and their dilutions are listed in Table S1.) Samples were then washed with PBS
601 thrice for 5 min durations at RT and then incubated with the respective secondary antibody and
602 Hoechst33342 diluted in the blocking solution for 30 min at RT. The secondary antibody was
603 subsequently washed with PBS, and the samples were mounted in the Crystal mount (Biomedica,

604 M02). All steps were performed with gentle shaking. Images were acquired and processed with
605 the Leica TCS SP8 Confocal microscope system.

606

607 **RT-PCR analysis of gene expression**

608 Total RNA was isolated from hSCOs using Trizol (Invitrogen) or the RNeasy Mini kit
609 RNase-Free DNase set (QIAGEN) in triplicate according to the manufacturer's instructions.
610 Isolated RNA (1 μ g) was used to synthesize cDNAs using Murine Moloney Leukemia Virus
611 reverse transcriptase (MMLV, Promega). Subsequently, cDNAs were amplified with gene-
612 specific primers (Sequence of primers are listed in Table S2). PCR conditions and the number
613 of cycles (25–35) were optimized as follows: 95°C for 15 min, denaturation at 95°C for 30 s,
614 annealing at 58–60°C for 30 s, and extension at 72°C for 30 s. qRT-PCR (Applied Biosystems,
615 ABI7500) analysis was performed using the SYBR GREEN master mix (Enzynomics or Elpis)
616 in combination with specific primers. The reactions were performed with an Eppendorf
617 Realplex4 cyler (Eppendorf). All values were normalized to GAPDH expression for
618 calculating the fold change.

619

620 **Machine learning**

621 The dataset was acquired on JuLi™Stage (NanoEntek) with a 4x objective lens. In pre-
622 processing, raw images were cropped into 512x512 pixel windows except for the background.

623 This step was automatically proceeded by the brightness distribution of the image. To
624 minimized batch effects arising from the differences in brightness/contrast, the pixel values
625 were normalized with even distribution. Of the total dataset comprising over 12,000 images,
626 we used 90% for training and 10% for validation at each morphological stage. In the training
627 set, image augmentation was used to increase the dataset size by randomly applying rotation,
628 translocation, flipping, zooming in, and zooming out. Model design and training were
629 performed using a convolutional neural network (CNN) in Tensorflow 1.13. The architecture
630 of the CNN model consisted of 5 convolution layers, max-pooling, and 2 fully connected layers.
631 To improve CNN classifier performance, the culture day-information was reflected as metadata
632 by One-Hot encoding. Finally, the classification results of morphological stages were presented
633 as 1 (neural tube), 2 (neural folding), or 3 (neural tube) as well as the class activation mapping
634 (CAM) to visually validate images along with the prediction scores.

635

636 **Electrophysiology**

637 To evaluate the functionality of the cultured hSCOs, we used a MEMS neural probe
638 integrated with 16 Pt microelectrodes and a microfluidic channel for neural signal recording
639 and localized drug delivery⁵¹. The following steps were performed: 1) To improve the recording
640 and stimulation capabilities, black Pt-coated microelectrodes (19 μm x 19 μm) were
641 employed⁵². 2) The impedance of black Pt-coated microelectrodes was measured in 0.1 M PBS
642 with a saturated calomel electrode using an impedance analyzer (nanoZ, Neuralynx). The
643 average impedance was 13 ± 1 k Ω at 1 kHz. To monitor neural activities of the organoid in an

644 incubator and inserting the neural probe into the organoid, we used a small-sized custom
645 microdrive system. The microdrive system consisted of 1) a PDMS recording chamber for the
646 loading of the organoid, 2) a microdrive for adjusting the vertical position of the neural probe,
647 and 3) an acrylic box for preventing rapid media evaporation in the incubator. After fixing the
648 neural probe on the microdrive using two screws (1 mm x 3 mm), we transferred the organoid
649 into the recording chamber. After positioning the organoid under the neural probe, the sample
650 was embedded in low-melt agarose, and then the neural probe was slowly inserted into the
651 organoid via the microdrive. The recording chamber was filled with a fresh DMEM/F12-based
652 culture media. After placing the organoid with the neural probe inserted into the acrylic box,
653 we measured the neural activities of the organoid in the incubator.

654 Signals recorded from 16 black Pt-coated microelectrodes were processed and digitized
655 using an RHD2132 amplifier board connected to an RHD2000 Evaluation System (20 kS s⁻¹
656 per channel, 300 Hz high pass filter, 6 kHz low pass filter, 16-bit ADC for spike recording, 20
657 kS s⁻¹ per channel, 0.3 Hz high pass filter, 3 kHz low pass filter, 16-bit ADC for fEPSP
658 recording). Spontaneous neural activity was recorded for at least 10 min and from at least 3
659 organoids. Additionally, to deliver drugs (TTX, CNQX/AP5, Bicuculine, Baclofen, CGRP) to
660 the sites where neural activity was measured in hSCOs, we used embedded microfluidic
661 channels in the neural probe. For a faster response time, a pressure-driven drug delivery system
662 was used. An electro-pneumatic regulator (ITV0051-2BL, SMC Pneumatics, Tokyo, Japan)
663 was connected to a nitrogen tank to control the precise input pressure. After monitoring
664 spontaneous neural activities of the hSCOs, 1.5 μ L of fresh medium was administered with the
665 drug for 3 min at a flow rate of 500 nL/min, and the change in neural activity following the

666 injection was monitored for 3 min. In this experiment, we used 6 μM TTX, 100 μM CNQX,
667 100 μM AP5, 10 μM bicuculline, 100 μM baclofen, and 1 μM α -CGRP. For measurements of
668 the evoked activity by electrical stimulation and short-term plasticity (STP), A365 stimulus
669 isolator (WPI, Sarasota, FL, USA) was used for electrical stimulation. Some of the
670 microelectrodes on the neural probe were used as stimulating electrodes. Evoked activity and
671 STP were induced by 1 train of HFS (20 pulses 100 Hz, 200 μs , 100 μA for evoked activity,
672 100 pulses 100 Hz, 200 μs , 100 μA for STP). In the case of STP measurement, neurons in the
673 hSCOs were stimulated by single pulses (50 μA , 200 μs pulse width, 30 s inter-pulse interval)
674 before and after HFS for fEPSP recording.

675 To detect neural activities from recorded signals, we used a custom Matlab spike-sorting
676 algorithm³⁵. The threshold amplitude (75 μV) was set at more than three times the noise level
677 (~ 25 μV). Burst activities among the detected neural signals were analyzed using the ISIN-
678 threshold method (ISI threshold: 0.1 sec, minimum number of spikes: 3)⁵³. The synchronized
679 activity between electrodes was analyzed using Pyspike ([https://github.com/mariomulansky](https://github.com/mariomulansky/PySpike)
680 /PySpike).

681

682 **Scanning electron microscopy and transmission electron microscopy**

683 Samples were fixed with 2.5% glutaraldehyde in 0.1 M phosphate buffer at 4°C for 2 h
684 before being washed with 0.1 M phosphate buffer thrice at RT. Fixed hSCOs were then
685 subjected to a secondary fixation procedure—they were soaked in 1% osmium tetroxide in 0.1

686 M phosphate buffer for 90 min at RT. Subsequently, hSCOs were dehydrated via a series of
687 ethanol (60%, 70%, 80%, 90%, and 95%) washes for 15 min each, followed by three washes
688 with absolute ethanol with the duration of 30 min at RT. Dehydrated hSCOs were immersed in
689 tert-Butyl alcohol twice for 20 min each at RT. Subsequently, hSCOs were frozen at -70°C
690 and freeze-dried to remove tert-Butyl alcohol. Finally, hSCOs were mounted on the top of a
691 sample holder with carbon tape, coated with platinum, and viewed under a scanning electron
692 microscope (Hitachwe S-4700, Hitachwe High-Technologies Corporation, Tokyo, Japan).

693 For transmission electron microscopy (TEM), hSCOs were pre-fixed with 2% PFA and 2.5%
694 glutaraldehyde in 0.1M phosphate buffer (pH 7.4) at RT for 1 h. Fixed hSCOs were then washed
695 twice with 0.1M phosphate buffer (pH 7.4) and post-fixed with 1% osmium tetroxide in 0.1M
696 phosphate buffer (pH 7.4) for 1 h at RT. To increase the image contrast, en bloc staining was
697 performed with 0.1% uranyl acetate in 50% ethanol for 1 h. Subsequently, the hSCOs were
698 dehydrated via an ascending ethanol series, followed by embedding in Epon812 (Okenshoji,
699 Japan) and polymerization in a dry oven (65°C , 48 h). Tissues were sectioned (70 nm) using
700 an EM UC7 ultra-microtome (Leica), mounted onto 200-mesh copper grids, and stained with
701 2% uranyl acetate and lead citrate for 5 min each. Sections were observed by TEM (Hitachwe
702 H-7650, Hitachwe High-Technologies Corporation, Tokyo, Japan).

703

704 **Single-cell RNA sequencing**

705 The hSCOs were collected in a petri dish on day 29 and chopped into small pieces. After

706 dissection, the hSCOs were dissociated by using papain containing L-cysteine by incubation at
707 37°C with gentle shaking. Papain was removed after 30 min, and the dissociated cells were
708 washed twice with ice-cold HBSS. Libraries were prepared using the Chromium controller
709 according to the 10x Single Cell 3' v3 protocol (10x Genomics). Briefly, the dissociated cell
710 suspensions were diluted in nuclease-free water to achieve a targeted cell count of 10,000. The
711 cell suspension was mixed with a master mix and loaded with Single-Cell 3' Gel Beads and
712 Partitioning Oil into a Single Cell 3' Chip. RNA transcripts from single cells were uniquely
713 barcoded and reverse-transcribed within droplets. cDNA molecules were pooled, and the cDNA
714 pool then went through an end repair process, followed by the addition of a single 'A' base and
715 ligation of the adapters. The products are then purified and enriched with PCR to develop the
716 final cDNA library. The purified libraries were quantified using qPCR based on the qPCR
717 Quantification Protocol Guide (KAPA) and qualified using the Agilent Technologies 4200
718 TapeStation (Agilent technologies). The libraries were subsequently sequenced using the
719 HiSeq platform (Illumina) with 33,000 reads/cell.

720

721 **Preprocessing and analysis of single-cell RNA-Seq data**

722 The raw sequence data were processed using the Cell Ranger pipeline (version 3.1.0, 10x
723 Genomics). Reads were aligned to the GRCh38 human genome reference using the STAR
724 aligner (version 2.5.1b)⁵⁴. Gene expression matrices were generated using the Seurat package
725 (version 3.1.5)⁵⁵ in R. Unless otherwise stated, we used functions of the Seurat package for

726 downstream analysis. Several quality-control steps were performed to filter out unreliable cells
727 and genes as follows: (i) removal of cells with >10 % of counts that were mapped to
728 mitochondrial genes, (ii) removal of cells with more than 7,000 or fewer than 200 unique
729 expressed genes, (iii) removal of genes detected in <10 cells. After the quality control
730 procedure, we obtained 18,365 genes across 11,038 cells for further analyses.

731 For downstream analysis, the UMI count data were normalized and variance-stabilized using
732 the R package SCTransform⁵⁶. The effect of mitochondrial gene expression was removed
733 during the normalization process. Highly variable genes were selected based on the variance
734 of Pearson residuals from normalized negative binomial regression. A graph-based clustering
735 algorithm (FindClusters function of Seurat) was used for single-cell clustering. The t-
736 Stochastic Neighbor Embedding (tSNE) visualization was achieved using the top 20 principal
737 components obtained from principal component analysis based on the elbow plot and
738 jackStraw score.

739 To identify the neuronal cell types, each cluster was annotated with the average expression
740 value of known marker genes for each cell type from previous studies^{57, 58}.

741

742 **Microarray**

743 Human spinal cord tissues derived from gestational week 18 were obtained with a protocol
744 approved by the Institutional Review Board committees at Chonnam National University
745 Hospital and Gwangju Institute of Science and Technology. The hSCO samples were prepared
746 based on the protocol described above. RNA purity and integrity were evaluated using an ND-

747 1000 Spectrophotometer (NanoDrop, Wilmington, USA) and Agilent 2100 Bioanalyzer
748 (Agilent Technologies, Palo Alto, USA). The Affymetrix Whole Transcript Expression array
749 process was executed according to the manufacturer's protocol (GeneChip Whole Transcript
750 PLUS reagent Kit). cDNA was synthesized using the GeneChip WT (Whole Transcript)
751 amplification kit as described by the manufacturer. The sense cDNA was then fragmented and
752 biotin-labeled with TdT (terminal deoxynucleotidyl transferase) using the GeneChip WT
753 Terminal labeling kit. Approximately 5.5 μ g of labeled DNA target was hybridized to the
754 Affymetrix GeneChip Human 2.0 ST Array at 45°C for 16 h. Hybridized arrays were washed
755 and stained on a GeneChip Fluidics Station 450 and scanned with a GCS3000 Scanner
756 (Affymetrix). Signal values were computed using the Affymetrix® GeneChip™ Command
757 Console software.

758 The data were normalized with a robust multi-average (RMA) method implemented in
759 Affymetrix® Power Tools (APT). We have focused on genes variable along with cellular
760 differentiation toward the spinal cord development on hSCO samples. Variable genes were
761 identified by calculating the median absolute deviation (MAD) across all hSCO samples with
762 the cutoff of top 5% of MAD values, which resulted in 1,365 genes. For comparison with the
763 human fetal spinal cord, Hierarchical cluster analysis was performed on the previously found
764 1,365 variable genes with all hSCO samples and the human fetal spinal cord sample. The
765 variable genes were divided into two clusters, up- and down-regulated genes on differentiation,
766 which were used for analyzing functional enrichment in the GO terms or biological processes.

767

768 **Chick notochord culture**

769 Fertilized eggs (Pulmuone) were incubated at 37 °C in a humidified incubator to obtain HH
770 25-27. The embryos were removed from the eggs and washed in ice-cold PBS. The intact
771 notochords were dissected and divided into several parts under a dissection microscope. Each
772 notochord fragment was transferred into a 96-well plate containing the day 7 organoid. The
773 organoids with chick notochord were cultured in DM containing 0.1 μM RA for 8 days. On
774 day 15, the organoids were grown in DM supplemented with bone morphogenetic protein 4
775 (BMP4) (50 ng/mL, PeproTech) or Purmorphamine (1 μM, Merck) for 6 days. The medium
776 was changed every alternate day.

777

778 **Neuromuscular junction formation**

779 Human skeletal muscle cells (hSkMCs) were purchased from PromoCell (C-12530). The 3D
780 myotube of the hSkMC formation protocol has been previously described⁵⁹. Briefly, hSkMCs
781 were seeded at a high density in the device and cultured in skeletal muscle cell growth medium
782 (PromoCell, C-23060) for 2 days. The growth medium was then replaced with skeletal muscle
783 cell differentiation medium (PromoCell, C-23061). After 7 days, when cells had formed a
784 condensed myotube, the medium was switched back to the growth medium to allow for the
785 stable differentiation of hSkMCs. On day 26, the developing hSCOs were cultured with
786 purmorphamine (Day 15) and plated on the 3D hSkMC myotube in differentiation medium for
787 hSCO. The co-culture medium was changed every 3 days. The hSCOs and myotubes were
788 fixed on day 38 of the co-culture.

789

790 **Dorsal root ganglion (DRG) culture**

791 DRGs were isolated from all levels of the spinal cord of Thy1-YFP mice (P7). After exposing
792 the spinal cord, DRGs were dissected with a dissection microscope and collected in a petri dish
793 filled with ice-cold HBSS. DRG explants were prepared by trimming nerve roots and removing
794 the connective tissue sheath with microsurgical scissors. Each DRG explant was placed with a
795 single hSCO in a round-bottom well of a 96-well plate. After 7 days, the fused hSCOs-DRG
796 complexes were transferred to the petri dish. For all procedures, the samples were cultured in
797 a 1:1 mixture of DMEM/F-12 and neurobasal medium as described above.

798

799 **Statistical analysis**

800 Statistical analyses were performed using an unpaired Student's t-test. All analyses were
801 performed with GraphPad Prism 8 software, and the results are presented as mean \pm SEM. P
802 values <0.05 were considered statistically significant.

803

804 **Ethical statements**

805 The human PSC study was approved by the Korea University Institutional Review Board.
806 All animal maintenance and experimental procedures were approved by members of the
807 Laboratory Animal Research Center at Korea University College of Medicine.

808

809 **Acknowledgments**

810 We would like to thank the Korea Basic Science Institute, Korea Brain Research Institute,
811 Dr. Kyung-Sook Yang and Ms. Jieun Na, in particular, for technical support. We also thank
812 Prof. Jung Hosung (Yonsei University) for critical comments. This research was supported by
813 the Brain Research Program through the National Research Foundation (NRF), which is funded
814 by the Korean Ministry of Science, ICT & Future Planning (NRF-2015M3C7A1028790, NRF-
815 2017M3C7A1047654, and NRF-2017M3A9B3061308).

816

817 **Author Contributions**

818 **Ju-Hyun Lee:** Conceptualization, Methodology, Validation, Investigation, Visualization,
819 Formal analysis, Writing - Original Draft, Writing - review & editing. **Hyogeun Shin:**
820 Methodology, Investigation, Resources, Visualization. **Mohammed R. Shaker:** Validation,
821 Investigation. **Hyun Jung Kim:** Methodology, Investigation. **June Hoan Kim:** Data Curation.
822 **Namwon Lee:** Software, Resources, Data Curation, Formal analysis. **Minjin Kang:**
823 Investigation, Resources. **Subin Cho:** Software, Resources, Visualization, Data Curation,
824 Formal analysis. **Tae Hwan Kwak:** Resources. **Jong Woon Kim:** Resources. **Mi-Ryong Song:**
825 Resources. **Seung-Hae Kwon:** Resources. **Dong Wook Han:** Resources. **Sanghyuk Lee:**
826 Resources. **Se-Young Choi:** Conceptualization. **Im Joo Rhyu:** Resources. **Hyun Kim:**
827 Resources. **Dongho Geum:** Conceptualization, Resources. **Il-Joo Cho:** Conceptualization,
828 Resources. **Woong Sun:** Conceptualization, Supervision, Project administration, Funding

829 acquisition, Writing - original draft, Writing - review & editing.

830

831 **Competing interests**

832 The authors declare no competing interests. The author N.L. is employed by InterMinds.

833

834 **Code availability**

835 The code for training the deep-learning models in this study are available at

836 <https://github.com/im-namwon/stemcell-classification>.

837

838

839

840

841

842

843

844

845

846 **References**

847

- 848 1. Smith, J.L. & Schoenwolf, G.C. Neurulation: coming to closure. *Trends in neurosciences* **20**,
849 510-517 (1997).
- 850 2. Jankowska, E. Spinal interneuronal systems: identification, multifunctional character and
851 reconfigurations in mammals. *The Journal of physiology* **533**, 31-40 (2001).
- 852 3. Lu, D.C., Niu, T. & Alaynick, W.A. Molecular and cellular development of spinal cord
853 locomotor circuitry. *Frontiers in molecular neuroscience* **8**, 25 (2015).
- 854 4. Juriloff, D.M. & Harris, M.J. Mouse models for neural tube closure defects. *Human molecular*
855 *genetics* **9**, 993-1000 (2000).
- 856 5. Greene, N.D., Stanier, P. & Copp, A.J. Genetics of human neural tube defects. *Human*
857 *molecular genetics* **18**, R113-R129 (2009).
- 858 6. Holmes, L.B. et al. The teratogenicity of anticonvulsant drugs. *New England Journal of*
859 *Medicine* **344**, 1132-1138 (2001).
- 860 7. Loeken, M.R. in *American Journal of Medical Genetics Part C: Seminars in Medical Genetics*,
861 Vol. 135 77-87 (Wiley Online Library, 2005).
- 862 8. Matok, I. et al. Exposure to folic acid antagonists during the first trimester of pregnancy and
863 the risk of major malformations. *British journal of clinical pharmacology* **68**, 956-962 (2009).
- 864 9. Mølgaard-Nielsen, D. & Hviid, A. Newer-generation antiepileptic drugs and the risk of major
865 birth defects. *Jama* **305**, 1996-2002 (2011).
- 866 10. Warmflash, A., Sorre, B., Etoc, F., Siggia, E.D. & Brivanlou, A.H. A method to recapitulate early
867 embryonic spatial patterning in human embryonic stem cells. *Nature methods* **11**, 847-854
868 (2014).
- 869 11. Haremake, T. et al. Self-organizing neuruloids model developmental aspects of Huntington's
870 disease in the ectodermal compartment. *Nature biotechnology* **37**, 1198-1208 (2019).
- 871 12. Moris, N. et al. An in vitro model of early anteroposterior organization during human
872 development. *Nature*, 1-6 (2020).
- 873 13. Kim, J., Koo, B.-K. & Knoblich, J.A. Human organoids: model systems for human biology and
874 medicine. *Nature Reviews Molecular Cell Biology* **21**, 571-584 (2020).
- 875 14. Lancaster, M.A. et al. Cerebral organoids model human brain development and microcephaly.
876 *Nature* **501**, 373 (2013).
- 877 15. Jo, J. et al. Midbrain-like organoids from human pluripotent stem cells contain functional
878 dopaminergic and neuromelanin-producing neurons. *Cell stem cell* **19**, 248-257 (2016).

48

- 879 16. Qian, X. et al. Brain-region-specific organoids using mini-bioreactors for modeling ZIKV
880 exposure. *Cell* **165**, 1238-1254 (2016).
- 881 17. Quadrato, G. et al. Cell diversity and network dynamics in photosensitive human brain
882 organoids. *Nature* **545**, 48 (2017).
- 883 18. Paşca, A.M. et al. Functional cortical neurons and astrocytes from human pluripotent stem
884 cells in 3D culture. *Nature methods* **12**, 671 (2015).
- 885 19. Kadoshima, T. et al. Self-organization of axial polarity, inside-out layer pattern, and species-
886 specific progenitor dynamics in human ES cell-derived neocortex. *Proceedings of the*
887 *National Academy of Sciences* **110**, 20284-20289 (2013).
- 888 20. Meinhardt, A. et al. 3D reconstitution of the patterned neural tube from embryonic stem
889 cells. *Stem cell reports* **3**, 987-999 (2014).
- 890 21. Ogura, T., Sakaguchi, H., Miyamoto, S. & Takahashi, J. Three-dimensional induction of dorsal,
891 intermediate and ventral spinal cord tissues from human pluripotent stem cells.
892 *Development* **145**, dev162214 (2018).
- 893 22. Hor, J.H. et al. Cell cycle inhibitors protect motor neurons in an organoid model of Spinal
894 Muscular Atrophy. *Cell death & disease* **9**, 1-12 (2018).
- 895 23. Martins, J.-M.F. et al. Self-organizing 3D human trunk neuromuscular organoids. *Cell stem*
896 *cell* **26**, 172-186. e176 (2020).
- 897 24. Rifès, P. et al. Modeling neural tube development by differentiation of human embryonic
898 stem cells in a microfluidic WNT gradient. *Nature Biotechnology*, 1-9 (2020).
- 899 25. Quadrato, G., Brown, J. & Arlotta, P. The promises and challenges of human brain organoids
900 as models of neuropsychiatric disease. *Nature medicine* **22**, 1220 (2016).
- 901 26. Velasco, S. et al. Individual brain organoids reproducibly form cell diversity of the human
902 cerebral cortex. *Nature*, 1 (2019).
- 903 27. Denham, M. et al. Multipotent caudal neural progenitors derived from human pluripotent
904 stem cells that give rise to lineages of the central and peripheral nervous system. *Stem Cells*
905 **33**, 1759-1770 (2015).
- 906 28. Anderson, M.J. et al. TCreERT2, a transgenic mouse line for temporal control of Cre-mediated
907 recombination in lineages emerging from the primitive streak or tail bud. *PloS one* **8**, e62479
908 (2013).
- 909 29. Nagai, T. et al. The Expression of the MouseZic1, Zic2, andZic3Gene Suggests an Essential
910 Role forZicGenes in Body Pattern Formation. *Developmental biology* **182**, 299-313 (1997).
- 911 30. Aaku-Saraste, E., Hellwig, A. & Huttner, W.B. Loss of occludin and functional tight junctions,
912 but not ZO-1, during neural tube closure—remodeling of the neuroepithelium prior to
913 neurogenesis. *Developmental biology* **180**, 664-679 (1996).

- 914 31. Nishimura, T., Honda, H. & Takeichi, M. Planar cell polarity links axes of spatial dynamics in
915 neural-tube closure. *Cell* **149**, 1084-1097 (2012).
- 916 32. Bretzner, F. & Brownstone, R.M. Lhx3-Chx10 reticulospinal neurons in locomotor circuits.
917 *Journal of Neuroscience* **33**, 14681-14692 (2013).
- 918 33. Floyd, T.L., Dai, Y. & Ladle, D.R. Characterization of calbindin D28k expressing interneurons
919 in the ventral horn of the mouse spinal cord. *Developmental Dynamics* **247**, 185-193 (2018).
- 920 34. Dale, N. Reciprocal inhibitory interneurons in the *Xenopus* embryo spinal cord. *The Journal*
921 *of Physiology* **363**, 61-70 (1985).
- 922 35. Shin, H. et al. Multifunctional multi-shank neural probe for investigating and modulating
923 long-range neural circuits in vivo. *Nature communications* **10**, 1-11 (2019).
- 924 36. Suzue, T. Respiratory rhythm generation in the in vitro brain stem-spinal cord preparation
925 of the neonatal rat. *The Journal of physiology* **354**, 173-183 (1984).
- 926 37. Hanson, M.G. & Landmesser, L.T. Characterization of the circuits that generate spontaneous
927 episodes of activity in the early embryonic mouse spinal cord. *Journal of Neuroscience* **23**,
928 587-600 (2003).
- 929 38. Saito, A. et al. Modulation of neuronal network activity using magnetic nanoparticle-based
930 astrocytic network integration. *Biomater Sci* **3**, 1228-1235 (2015).
- 931 39. Zafeiriou, M.-P. et al. Developmental GABA polarity switch and neuronal plasticity in
932 Bioengineered Neuronal Organoids. *Nature Communications* **11**, 1-12 (2020).
- 933 40. Greene, N.D. & Copp, A.J. Neural tube defects. *Annual review of neuroscience* **37**, 221-242
934 (2014).
- 935 41. Agopian, A., Tinker, S.C., Lupo, P.J., Canfield, M.A. & Mitchell, L.E. Proportion of neural tube
936 defects attributable to known risk factors. *Birth Defects Research Part A: Clinical and*
937 *Molecular Teratology* **97**, 42-46 (2013).
- 938 42. Weston, J. et al. Monotherapy treatment of epilepsy in pregnancy: congenital malformation
939 outcomes in the child. *Cochrane Database of Systematic Reviews* (2016).
- 940 43. Kawada, J. et al. Generation of a motor nerve organoid with human stem cell-derived
941 neurons. *Stem cell reports* **9**, 1441-1449 (2017).
- 942 44. Sternfeld, M.J. et al. Speed and segmentation control mechanisms characterized in
943 rhythmically-active circuits created from spinal neurons produced from genetically-tagged
944 embryonic stem cells. *Elife* **6**, e21540 (2017).
- 945 45. Zheng, Y. et al. Dorsal-ventral patterned neural cyst from human pluripotent stem cells in a
946 neurogenic niche. *Science advances* **5**, eaax5933 (2019).
- 947 46. Davidson, B.P., Kinder, S.J., Steiner, K., Schoenwolf, G.C. & Tam, P.P. Impact of node ablation
948 on the morphogenesis of the body axis and the lateral asymmetry of the mouse embryo

- 949 during early organogenesis. *Developmental biology* **211**, 11-26 (1999).
- 950 47. Stemple, D.L. Structure and function of the notochord: an essential organ for chordate
951 development. *Development* **132**, 2503-2512 (2005).
- 952 48. Moury, J.D. & Schoenwolf, G.C. Cooperative model of epithelial shaping and bending during
953 avian neurulation: autonomous movements of the neural plate, autonomous movements of
954 the epidermis, and interactions in the neural plate/epidermis transition zone. *Developmental*
955 *dynamics* **204**, 323-337 (1995).
- 956 49. Sato, T. et al. Single Lgr5 stem cells build crypt-villus structures in vitro without a
957 mesenchymal niche. *Nature* **459**, 262 (2009).
- 958 50. Yoon, S.-J. et al. Reliability of human cortical organoid generation. *Nature methods* **16**, 75-
959 78 (2019).
- 960 51. Shin, H. et al. Neural probes with multi-drug delivery capability. *Lab on a Chip* **15**, 3730-
961 3737 (2015).
- 962 52. Lee, Y.J., Song, K.-I., Kang, J.Y. & Lee, S.H. in 2015 37th Annual International Conference of
963 the IEEE Engineering in Medicine and Biology Society (EMBC) 3415-3418 (IEEE, 2015).
- 964 53. Bakkum, D.J. et al. Parameters for burst detection. *Frontiers in computational neuroscience*
965 **7**, 193 (2014).
- 966 54. Dobin, A. et al. STAR: ultrafast universal RNA-seq aligner. *Bioinformatics* **29**, 15-21 (2013).
- 967 55. Butler, A., Hoffman, P., Smibert, P., Papalexi, E. & Satija, R. Integrating single-cell
968 transcriptomic data across different conditions, technologies, and species. *Nature*
969 *biotechnology* **36**, 411-420 (2018).
- 970 56. Hafemeister, C. & Satija, R. Normalization and variance stabilization of single-cell RNA-seq
971 data using regularized negative binomial regression. *Genome biology* **20**, 1-15 (2019).
- 972 57. Rosenberg, A.B. et al. Single-cell profiling of the developing mouse brain and spinal cord
973 with split-pool barcoding. *Science* **360**, 176-182 (2018).
- 974 58. Delile, J. et al. Single cell transcriptomics reveals spatial and temporal dynamics of gene
975 expression in the developing mouse spinal cord. *Development* **146** (2019).
- 976 59. Sakar, M.S. et al. Formation and optogenetic control of engineered 3D skeletal muscle
977 bioactuators. *Lab on a Chip* **12**, 4976-4985 (2012).
- 978